Reflection tomography of time-lapse GPR data for studying dynamic unsaturated flow phenomena

Adam R. Mangel[1,2], Stephen M.J. Moysey[2], John Bradford[1]

[1] Department of Geophysics, Colorado School of Mines, Golden, Colorado, 80401, USA
[2] Department of Environmental Engineering and Earth Science, Clemson University, Clemson, South Carolina, 29634, USA

Corresponding to: Adam R. Mangel (adam.mangel@pnnl.gov)

Abstract

Ground-penetrating radar (GPR) reflection tomography algorithms allow non-invasive monitoring of water content changes resulting from flow in the vadose zone. The approach requires multi-offset GPR data that are traditionally slow to collect. We automate GPR data collection to reduce the survey time significantly, thereby making this approach to hydrologic monitoring feasible. The method was evaluated using numerical simulations and laboratory experiments that suggest reflection tomography can provide water content estimates to within 5%-10% vol. vol.$^{-1}$ for the synthetic studies, whereas the empirical estimates were typically within 5%-15% of measurements from in-situ probes. Both studies show larger observed errors in water content near the periphery of the wetting front, beyond which additional reflectors were not present to provide data coverage. Overall, coupling automated GPR data collection with reflection tomography provides a new method for informing models of subsurface hydrologic processes and a new method for determining transient 2D soil moisture distributions.

1. Introduction

Preferential flow is ubiquitous in the vadose zone, occurring under a wide variety of conditions and over a broad range of scales (Nimmo, 2012). Reviews such as those by Hendrickx and Flury (2001) and Jarvis (2007) illustrate that a basic mechanistic understanding of preferential flow exists. Jarvis et al. (2016) point out, however, that we still lack models capable of reproducing empirical observations in the field and highlight the importance of non-invasive imaging techniques for improving this understanding. We suggest that ground-penetrating radar (GPR) reflection tomography could fill this need by quantitatively mapping changes in water content through space and time at the sub-meter scale.

Reflection GPR is commonly used to image subsurface structures, but is also well suited to understanding hydrologic variability due to the strong dependence of EM wave velocities on soil volumetric water content (Topp et al., 1980). As a result, GPR has been adapted to monitor variability in hydrologic processes at multiple scales through time and space in a variety of contexts (Buchner et al., 2011; Busch et al., 2013; Guo et al., 2014; Haarder et al., 2011; Lunt et al., 2005; Mangel et al., 2012, 2015b, 2017; Moysey, 2010; Saintenoy et al., 2007; Steelman and Endres, 2010; Vellidis et al., 1990). Note that GPR methods are not applicable in media with relatively high electrical conductivity.

While these studies have illustrated a variety of techniques for monitoring changes in water content within the subsurface, they have generally required assumptions to constrain the interpretation, such as the use of *a priori* information regarding subsurface structure (e.g., Lunt et al., 2005) or the GPR wave velocity (Haarder et al., 2011).

37   These limitations arise from the fact that GPR data are recorded as energy arriving at the receiver antenna as a function

38   of time. Inherent assumptions therefore exist in analyzing traveltime data collected with antennas separated by a fixed

39   offset because both the distance travelled by the GPR wave to a reflector and the velocity of the GPR wave are

40   unknown. It has been demonstrated that GPR data collected via a multi-offset survey can constrain both the depth to

41   a moving wetting front and the water content behind the front over the course of an infiltration event (Gerhards et al.,

42   2008; Mangel et al., 2012). The limitation of these studies, however, was that the authors assumed a 1D flow system

43   and that GPR data lacked information regarding lateral variability in soil moisture.

44   Extending multi-offset techniques (Forte and Pipan, 2017; Jaumann and Roth, 2017; Klenk et al., 2015;

45   Lambot et al., 2004, 2009) to image flow in the vadose zone requires an increase in the speed at which these data can

46   be collected and advanced processing methods that can combine thousands of measurements into spatially and

47   temporally variable water content estimates. We have recently overcome the data collection problem by automating

48   GPR data collection using a computer controlled gantry, thereby reducing the data collection time for large multi-

49   offset surveys from hours to minutes (Mangel et al., 2015a). Tomography and wave migration algorithms from

50   seismic literature have been available for decades (Baysal et al., 1983; Lafond and Levander, 1993; Sava and Biondi,

51   2004a, 2004b; Stork, 1992; Yilmaz and Chambers, 1984) and are being continually adapted to GPR applications. For

52   example, this work is made possible due to adaptation of the pre-stack migration algorithm (Leparoux et al., 2001)

53   and adaptation of the reflection tomography algorithm (Bradford, 2006) to multi-offset GPR data. Subsequent studies

54   have demonstrated the use of GPR reflection tomography for imaging static distributions of subsurface water content

55   with great detail (Bradford, 2008; Bradford et al., 2009; Brosten et al., 2009). The combination of automated GPR

56   data collection and reflection tomography makes time-lapse imaging of water content during infiltration a feasible

57   means to study flow in the vadose zone.

58   The objective of this study is to evaluate reflection tomography of high-resolution GPR data as a tool for

59   observing and characterizing unsaturated flow patterns during infiltration into a homogeneous soil. To evaluate the

60   efficacy of the algorithm for resolving dynamic soil water content in 2D, we first test the algorithm using numerical

61   simulations and compare the results to true water content distributions. We then apply the algorithm to time-lapse

62   GPR data collected during an infiltration and recovery event in a homogeneous soil and compare results to

63   measurements from in-situ soil moisture probes.

64   **2. Methods**

65   **2.1. The Reflection Tomography Algorithm**

66   The goal of reflection tomography is to determine a velocity model that best aligns migrated reflection

67   arrivals for a common reflection point across a set of source-receiver offsets. For brevity, we will limit our discussion

68   here to the key ideas and methods of the tomography algorithm; we refer the reader to Stork (1992) for the original

69   tomography algorithm and to Bradford (2006) for the application to GPR data.

70   The data required for this algorithm are an ensemble of common-midpoint (CMP) gathers collected along a

71   path. Given that GPR data is a time-series record of electromagnetic energy arriving at a point in space, we must

72   know the proper velocity structure to migrate the data and produce a depth registered image of the GPR energy.

73   Migration attempts to remove the hyperbolic trend of reflections with respect to antenna offset (Figure 1a) by using

74   the wave velocity to reposition reflections to the proper depth at which they occur. If CMP data are migrated with the

75   correct velocity, reflections from layers in the subsurface are flattened as a function of offset (Fig. 1c). If the velocity

76   estimate is incorrect, e.g. 10% too slow (Fig. 1b) or 10% too fast (Fig. 1d), the arrival is not flat and exhibits residual

77   moveout (RMO). To solve for the velocity structure and properly migrate the data, the reflection tomography

78   algorithm proceeds as follows (Bradford, 2006; Stork, 1992):

79   1.   Generate a starting depth vs. velocity model.

80   2.   Migrate the data with the starting velocity model and stack the data.

81   3.   Pick horizons on the stacked image.

82   4.   Perform ray-tracing to the picked horizons with the velocity model.

83   5.   Evaluate horizons for residual moveout.

84   6.   Adjust velocity model using reflection tomography.

85   7.   Apply revised velocity model using migration and quality check RMO.

86   8.   Iterate at step three if necessary.

87   For this work, starting velocity models for the tomography algorithm are determined by smoothing results

88   from 1D velocity analysis of individual CMPs (Neidell and Taner, 1971). The reflection tomography algorithm then

89   adjusts the velocity distribution until reflections in the depth corrected (i.e., migrated) data line up to produce a

90   reflection at a consistent depth across all traces in a CMP. Through sequential iterations of the tomographic inversion,

91   the RMO metric is reduced on a global scale. For this work, the reflection tomography was performed using the

92   SeisWorks software suite and Kirchhoff pre-stack depth migration (Yilmaz and Doherty, 2001).

93   **2.2. Experimental Setup and Procedure**

94   We used a 4 m x 4 m x 2 m tank for the controlled study of unsaturated flow phenomenon with GPR (Fig.

95   1e, f). We filled the tank with a medium-grained sand to a depth of 0.60 m. Below the sand was a 0.30 m layer of

96   gravel that acts as backfill for 16 individual drain cells that are pitched slightly toward central drains that route water

97   to outlets on the outside of the tank. We constructed an automated data collection system to allow for the high-speed

98   high-resolution collection of GPR data (Mangel et al., 2015a); the GPR gantry fits inside of the tank so the antennas

99   are in contact with the sand surface. All GPR data described here were collected along the y-axis of the tank at a fixed

100   position of x = 2.0 m, where the bottom of the tank is flat (Fig. 1e, f).

101   The automated system, which utilizes a 1000 MHz bistatic radar (Sensors and Software, Inc.), was operated

102   to obtain 101 CMPs spaced at 0.02 m intervals between y = 1.0 m - 3.0 m. Each CMP consisted of 84 traces with

103   offsets between 0.16 m-1.0 m at 0.01 m step size. Thus, a complete CMP data set for one observation time consists

104   of almost 8,500 individual GPR traces. With this configuration using the automated system, a CMP at a single location

105   could be collected in 1.8 seconds with a total cycle of CMP data locations collected every 3.9 minutes.

106   GPR data collection occurred prior to irrigation to evaluate background conditions. Data collection continued

107   during irrigation, which was applied at a flux of 0.125 cm min^{-1} for a duration of 2.13 hrs. Spatial heterogeneity in

108   the applied flux has been observed in laboratory testing of the irrigation equipment. Fifteen EC-5 soil moisture probes

109   (METER, Inc.) logged volumetric water content at 10-second intervals during the experiment (Fig. 1e, f). Note that

110   the soil moisture probes are located out of the plane of the GPR line by 0.5 m (Figure 1f). GPR data collection

111 continued for 40 minutes after the irrigation was terminated. In total, 45 complete sets of data were collected over the

112 course of the 3-hour experiment, yielding more than 500,000 GPR traces in the experimental data set.

2.3. Execution of the Numerical Simulations

114 We employed HYDRUS-2D (Simunek and van Genuchten, 2005) to simulate a theoretical and realistic

115 hydrologic response to an infiltration event using two different initial conditions: i) hydrostatic equilibrium leading to

116 a water content distribution controlled by the soil water retention curve, and ii) a uniform soil with a water content of

117 0.07. We selected the Mualem-van Genuchten soil model (Mualem, 1976) and parameterized the model as follows

118 based on hydraulic testing of the sand: residual water content (θ_r) = 0.06, saturated water content (θ_s) = 0.38, air-entry

119 pressure (α) = 0.058 cm^{-1}, shape parameter (n) = 4.09, and saturated hydraulic conductivity (K_s) = 4.6 cm min^{-1}. The

120 hydraulic conductivity for the homogeneous model was reduced to 1 cm min^{-1} to build a larger contrast of water

121 content across the wetting front. For all HYDRUS simulations, we used a constant flux boundary condition of 0.125

122 cm min^{-1} from y = 1.6 m - 2.4 m along the ground surface, set the model domain depth to 0.6 m, length to 4.0 m, and

123 nominal cell size to 0.04 m. Remaining nodes at the surface were set to no flow boundaries and lower boundary nodes

124 were set to a seepage face with the pressure head equal to zero.

125 We calculated relative dielectric permittivity values for the GPR simulations by transforming water content values

126 from HYDRUS-2D using the Topp equation (Topp et al., 1980). We used the magnetic permeability of free space for

127 the entire model domain and set electrical conductivity of the soil to 1 mS m^{-1}. Although electrical conductivity

128 changes as a function of the water content, these changes primarily influence wave attenuation, which is not significant

129 or accounted for in the processing performed with the SeisWorks software.

130 We performed GPR simulations in MATLAB using a 2D finite-difference time-domain code (Irving and

131 Knight, 2006). The GPR model domain was set to 4.0 m long and 1.1 m high with a cell size of 0.002 m. The lower

132 0.3 m of the domain was set to a relative dielectric permittivity of 2.25 to represent the lower gravel layer and the

133 upper 0.2 m was modeled as air to simulate the air-soil interface. Simulated data were collected as described in the

134 section detailing the tank experiment. For quick computation, simulations were deployed on the Palmetto

135 supercomputer cluster at Clemson University, where single source simulations ran in 20 minutes using nodes with 8

136 CPUs and 32 GB of RAM.

3. Reflection Tomography of Simulations

138 The HYDRUS-2D output shows the development of an infiltrating wetting front for the two scenarios with

139 differing initial conditions (Figs. 2a, f, k). For conditions prior to irrigation, the bottom of sand reflection (B) is

140 horizontal on the common-offset profile (COP) data indicating a constant velocity across the model domain (Fig. 2b).

141 Additionally, the CMPs show identical hyperbolic moveout, i.e., the offset vs. traveltime relationship, indicating a

142 homogeneous velocity across the model domain (Fig. 2c-e). The airwave and groundwave are also visible in the data,

143 but are not analyzed, or further discussed.

144 During infiltration, (B) is distorted at the center of the COP due to the decreased velocity caused by the

145 infiltrating water (Figs. 2g, l). A reflection from the infiltrating wetting front (W) is faintly visible for the model with

146 variable initial water contents (Fig. 2g) and comparatively strong for simulations with a dry background (Fig. 2l) due

147 to different levels of dielectric contrast across the wetting front in each case. CMPs also indicate perturbations in the

148 velocity field as the moveout changes dramatically when the wetted zone is encountered (Figs. 2h-j, m-o). A refraction

149 is also observed on the CMPs, which is a rare occurrence considering that GPR wave velocity typically decreases with

150 depth.

151 Prior to the onset of flow, the reflection tomography algorithm produces a uniform water content distribution

152 that agrees with the arithmetic average of the true water content but does not capture the vertical gradation observed

153 in Figure 3a. This is because information regarding vertical velocity variations is absent, i.e., more reflectors at

154 different depths are required to capture this variability. As a result, errors in the water content estimation exceed 10%

155 vol. vol.$^{-1}$ (Fig. 3d).

156 During infiltration, the wetting front is imaged relatively well for the case where the soil was initially dry

157 (Figs. 3i-l), particularly as the plume advances deeper into the subsurface (Figs. 3m-p) where there is improved data

158 coverage. The tomography algorithm overestimates the depth of the wetting front by roughly 0.10 m for the case

159 presented in Figure 3i-l, which is likely due to smoothing effects required to regularize the inversion or an error in the

160 picking of the wetting front horizon. Considerable errors in the tomography results persist, however, with the results

161 degrading further for the scenario with variable initial water content (Figs. 3e-h) given that reflection contrasts with

162 the wetting front are weaker. The presence of an additional reflector, however, increases the ability of the tomography

163 to resolve vertical variability, e.g. Figure 2g vs. Figure 2b. Overall, errors are reduced near reflectors to about 5% vol.

164 vol.$^{-1}$. These results suggest that water content changes resulting from unsaturated flow can be imaged and that as

165 more information becomes available in the form of additional reflections, the tomography results improve.

166 **4. Reflection Tomography of Experimental Data**

167 At initial conditions, the sand layer reflection (B) is visible at 10 ns traveltime in the COP collected over the

168 imaging area (Fig. 4a). Normal hyperbolic moveout of (B) is observed on the CMPs (Fig.4b, c, d). These results are

169 qualitatively identical to observations from numerical simulations (Figs. 2b-e).

170 During infiltration, the water content of the sand layer increases substantially (Fig. 5) and longer traveltimes

171 for the arrivals on the COP data are observed near the center of the tank (Figs. 4f, i). Rather than a coherent reflection

172 for the wetting front (W) (Fig. 2l), multiple discrete reflections are present in the COP data (Fig. 4e, i, m) indicating

173 a heterogeneous wetting of the soil. These reflections are difficult to identify on the CMPs given the complex moveout

174 pattern (Fig. 4i) but are more easily identified in animations of COP projections of the data (included as a

175 supplementary file). Analysis of the data was greatly aided by the animation of the data and the pre-stack migration

176 algorithm, which stacks the data over all offsets to produce a coherent image of reflectors with an increased signal to

177 noise ratio. Heterogeneous wetting of the soil is also very pronounced in the soil-moisture probe data with many of

178 the probes responding out of sequence with depth (Fig 5). After irrigation, the soil moisture probes show a decrease

179 in the soil water content (Fig. 5) apart from one probe (Fig. 5c) and the GPR data show a slight decrease in the

180 traveltime to the bottom of sand reflection (Figs. 4k-n).

181 The tomographic imaging results from the initial GPR data set collected prior to irrigation agree with data

182 from soil moisture probes which indicates an average soil moisture of roughly 5% during this time (Figs. 4e, 5).

183 During infiltration and recovery, tomographic images of the tank show a wet zone at the center and relatively dry

184 edges outside the irrigated area (Figs. 4j, o). Overall, the tomography results near the center of the tank are within

185 10% vol. vol.$^{-1}$ of the soil moisture data and show a non-uniform wetting of the soil during infiltration that was not
186 observed in the numerical study, suggesting the occurrence of preferential flow. Errors in the estimates of water
187 content near the edges of the advancing plume exceed 15% vol. vol.$^{-1}$ (Fig. 4b, c), though the general patterns in
188 wetting are consistent. After irrigation, the tomography results on the edges of the wetted zone are in better agreement
189 with the soil moisture probe data, but less spatial information is available given the lack of a wetting front reflection
190 (Fig. 4o).

5. Conclusions

192 Reflection tomography in the post-migrated domain is a viable method for resolving transient soil moisture
193 content in 2D associated with an infiltration and recovery event in a homogeneous soil. Reflection tomography of
194 numerical data produced water content distributions that were in good agreement with true water content values from
195 the simulations. The tomography was generally able to match the true water content values to within 5% -10% vol.
196 vol.$^{-1}$. However, distinct migration artifacts were produced around the edges of the wetting front, especially for cases
197 where the initial water content was non-uniform, obscuring details about the shape of the wetted region. Analysis of
198 data collected in a sand tank proved to be more difficult, however, the tomography was able to produce hydrologically
199 realistic distributions of water content in space and time that were generally within 5% -15% vol. vol.$^{-1}$ of
200 measurements from in-situ soil moisture probes. These discrepancies may have to do with reduction in available
201 reflections for analysis caused by the heterogeneous flow response compared to the coherent wetting front reflection
202 seen in the numerical experiment, e.g. the complex distribution of the wetted soil as a result of heterogenous
203 distribution of water at the surface, texture variability in the soil, or other preferential flow mechanisms (Jarvis et al.,
204 2016). The distance between the location of the CMPs and the moisture probes and the difference in measurement
205 scale between the two methods may also be a source of these discrepancies given the evidence of non-uniform flow.
206 Regardless, the fact that the GPR data were able to capture this heterogeneity is an impressive feat given that
207 tomographic imaging operated independently of any hydrologic information and provided evidence that our
208 conceptual model was not representative of the physical system.

209 Regardless of discrepancies observed between the GPR and probe water content values, it is evident that
210 automated high-speed GPR data acquisition coupled with reflection tomography algorithms can provide a new
211 approach to hydrologic monitoring. Testing and revision of conceptual hydrologic models regarding non-uniform
212 flow in the vadose zone demands such non-invasive time-lapse imaging data. Artifacts observed in the numerical
213 simulation results, however, suggest that improvements in this methodology could be achieved. While there are likely
214 fundamental limitations to the information content of the data, the Kirchhoff pre-stack depth migration algorithm used
215 in this study could be replaced by more sophisticated algorithms like reverse-time migration (Baysal et al., 1983)
216 which may reduce the observed imaging artifacts. Additionally, results from the tomography algorithm may prove to
217 be beneficial as a precursor to higher-order inversion techniques, like full-waveform inversion, which requires detailed
218 starting models of velocity for convergence. Overall, coupling automated GPR data collection with reflection
219 tomography provides a new method for informing models of subsurface hydrologic processes and a new method for
220 determining transient 2D soil moisture distributions.

221   **6.   Acknowledgements**

222   This material is based upon work supported by, or in part by, the National Science Foundation under grant

223   number EAR-1151294. We also acknowledge Clemson University for generous allotment of compute time on

224   Palmetto cluster. Data used in this publication and a supplementary movie of the data are available through the

225   Colorado School of Mines at the following URL: https://hdl.handle.net/11124/172053. The authors declare that they

226   have no conflict of interest.

227   **7.   References**

228   Baysal, E., Kosloff, D. and Sherwood, J.: Reverse Time Migration, Geophysics, 48(11), 1514–1524,

229   doi:10.1190/1.1441434, 1983.

230   Bradford, J. H.: Applying reflection tomography in the postmigrated domain to multifold ground-penetrating radar

231   data, Geophysics, 71(1), K1–K8, doi:10.1190/1.2159051, 2006.

232   Bradford, J. H.: Measuring water content heterogeneity using multifold GPR with reflection tomography, Vadose Zo.

233   J., 7(1), 184, doi:10.2136/vzj2006.0160, 2008.

234   Bradford, J. H., Clement, W. P. and Barrash, W.: Estimating porosity with ground-penetrating radar reflection

235   tomography: A controlled 3-D experiment at the Boise Hydrogeophysical Research Site, Water Resour. Res., 45(4),

236   n/a-n/a, doi:10.1029/2008WR006960, 2009.

237   Brosten, T. R., Bradford, J. H., McNamara, J. P., Gooseff, M. N., Zarnetske, J. P., Bowden, W. B. and Johnston, M.

238   E.: Multi-offset GPR methods for hyporheic zone investigations, Near Surf. Geophys., 7, 244–257, 2009.

239   Buchner, J. S., Kuhne, A., Antz, B., Roth, K. and Wollschlager, U.: Observation of volumetric water content and

240   reflector depth with multichannel ground-penetrating radar in an artificial sand volume, 2011 6th Int. Work. Adv. Gr.

241   Penetrating Radar, 1–5, doi:10.1109/IWAGPR.2011.5963910, 2011.

242   Busch, S., Weihermüller, L., Huisman, J. A., Steelman, C. M., Endres, A. L., Vereecken, H. and van der Kruk, J.:

243   Coupled hydrogeophysical inversion of time-lapse surface GPR data to estimate hydraulic properties of a layered

244   subsurface, Water Resour. Res., 49(12), 8480–8494, doi:10.1002/2013WR013992, 2013.

245   Forte, E. and Pipan, M.: Review of multi-offset GPR applications: Data acquisition, processing and analysis, Signal

246   Processing, 132, 1–11, doi:10.1016/j.sigpro.2016.04.011, 2017.

247   Gerhards, H., Wollschläger, U., Yu, Q., Schiwek, P., Pan, X. and Roth, K.: Continuous and simulataneous

248   measurement of reflector depth and average soil-water content with multichannel ground-penetrating radar,

249   Geophysics, 73(4), 15–23, 2008.

250   Gloaguen, E., Chouteau, M., Marcotte, D. and Chapuis, R.: Estimation of hydraulic conductivity of an unconfined

251   aquifer using cokriging of GPR and hydrostratigraphic data, J. Appl. Geophys., 47(2), 135–152, doi:10.1016/S0926-

252   9851(01)00057-X, 2001.

253   Guo, L., Chen, J. and Lin, H.: Subsurface lateral preferential flow network revealed by time-lapse ground-penetrating

254   radar in a hillslope, Water Resour. Res., 50, 9127–9147, doi:10.1002/2013WR014603, 2014.

255   Haarder, E. B., Looms, M. C., Jensen, K. H. and Nielsen, L.: Visualizing Unsaturated Flow Phenomena Using High-

256   Resolution Reflection Ground Penetrating Radar, Vadose Zo. J., 10(1), 84, doi:10.2136/vzj2009.0188, 2011.

257   Hendrickx, J. M. H. and Flury, M.: Uniform and Preferential Flow Mechanisms in the Vadose Zone, in Conceptual

258   Models of Flow and Transport in the Fractured Vadose Zone, pp. 149–187, National Academy Press, Washington,
259   D.C., 2001.

260   Irving, J. and Knight, R.: Numerical modeling of ground-penetrating radar in 2-D using MATLAB, Comput. Geosci.,
261   32(9), 1247–1258, doi:10.1016/j.cageo.2005.11.006, 2006.

262   Jarvis, N., Koestel, J. and Larsbo, M.: Understanding Preferential Flow in the Vadose Zone: Recent Advances and
263   Future Prospects, Vadose Zo. J., 15(12), 0, doi:10.2136/vzj2016.09.0075, 2016.

264   Jarvis, N. J.: A review of non-equilibrium water flow and solute transport in soil macropores: Principles, controlling
265   factors and consequences for water quality, Eur. J. Soil Sci., 58(3), 523–546, doi:10.1111/j.1365-2389.2007.00915.x,
266   2007.

267   Jaumann, S. and Roth, K.: Soil hydraulic material properties and subsurface architecture from time-lapse GPR,
268   Hydrol. Earth Syst. Sci. Discuss., (September), 1–34, doi:10.5194/hess-2017-538, 2017.

269   Klenk, P., Jaumann, S. and Roth, K.: Quantitative high-resolution observations of soil water dynamics in a complicated
270   architecture using time-lapse ground-penetrating radar, Hydrol. Earth Syst. Sci., 19(3), 1125–1139, doi:10.5194/hess-
271   19-1125-2015, 2015.

272   Lafond, C. F. and Levander, A. R.: Migration moveout analysis and depth focusing, Geophysics, 58(1), 91–100,
273   doi:10.1190/1.1443354, 1993.

274   Lambot, S., Antoine, M., van den Bosch, I., Slob, E. C. and Vanclooster, M.: Electromagnetic Inversion of GPR
275   Signals and Subsequent Hydrodynamic Inversion to Estimate Effective Vadose Zone Hydraulic Properties, Vadose
276   Zo. J., 3(4), 1072, doi:10.2136/vzj2004.1072, 2004.

277   Lambot, S., Slob, E., Rhebergen, J., Lopera, O., Jadoon, K. Z. and Vereecken, H.: Remote Estimation of the Hydraulic
278   Properties of a Sand Using Full-Waveform Integrated Hydrogeophysical Inversion of Time-Lapse, Off-Ground GPR
279   Data, Vadose Zo. J., 8(3), 743, doi:10.2136/vzj2008.0058, 2009.

280   Leparoux, D., Gibert, D. and Cote, P.: Adaptation of prestack migration to multi-offset ground-penetrating radar
281   (GPR) data, Geophys. Prospect., 49(3), 374–386, doi:10.1046/j.1365-2478.2001.00258.x, 2001.

282   Lunt, I. A., Hubbard, S. S. and Rubin, Y.: Soil moisture content estimation using ground-penetrating radar reflection
283   data, J. Hydrol., 307(1–4), 254–269, doi:10.1016/j.jhydrol.2004.10.014, 2005.

284   Mangel, A. R., Moysey, S. M. J., Ryan, J. C. and Tarbutton, J. A.: Multi-offset ground-penetrating radar imaging of
285   a lab-scale infiltration test, Hydrol. Earth Syst. Sci., 16(11), doi:10.5194/hess-16-4009-2012, 2012.

286   Mangel, A. R., Lytle, B. A. and Moysey, S. M. J.: Automated high-resolution GPR data collection for monitoring
287   dynamic hydrologic processes in two and three dimensions, Lead. Edge, 34(2), doi:10.1190/tle34020190.1, 2015a.

288   Mangel, A. R., Moysey, S. M. J. and van der Kruk, J.: Resolving precipitation induced water content profiles by
289   inversion of dispersive GPR data: A numerical study, J. Hydrol., 525, 496–505, doi:10.1016/j.jhydrol.2015.04.011,
290   2015b.

291   Mangel, A. R., Moysey, S. M. J. and van der Kruk, J.: Resolving infiltration-induced water content profiles by
292   inversion of dispersive ground-penetrating radar data, Vadose Zo. J., 16, doi:10.2136/vzj2017.02.0037, 2017.

293   Moysey, S. M.: Hydrologic trajectories in transient ground-penetrating-radar reflection data, Geophysics, 75(4),
294   WA211-WA219, doi:10.1190/1.3463416, 2010.

295   Mualem, Y.: A new model for predicting the hydraulic conductivity of unsaturated porous media, Water Resour. Res.,

296   12(3), 1976.

297   Neidell, N. S. and Taner, M. T.: Semblance and other coherency measures for multichannel data, Geophysics, 36(3),

298   482–497, 1971.

299   Nimmo, J. R.: Preferential flow occurs in unsaturated conditions, Hydrol. Process., 26(5), 786–789,

300   doi:10.1002/hyp.8380, 2012.

301   Saintenoy, A., Schneider, S. and Tucholka, P.: Evaluating GroundPenetrating Radar use for water infiltration

302   monitoring, 2007 4th Int. Work. on, Adv. Gr. Penetrating Radar, 91–95, doi:10.1109/AGPR.2007.386531, 2007.

303   Sava, P. and Biondi, B.: Wave-equation migration velocity analysis. I. Theory, Geophys. Prospect., 52(6), 593–606,

304   doi:10.1111/j.1365-2478.2004.00447.x, 2004a.

305   Sava, P. and Biondi, B.: Wave-equation migration velocity analysis — II : Subsalt imaging examples Geophysical

306   Prospecting , accepted for publication, , 1–36, 2004b.

307   Simunek, J. and van Genuchten, M. T.: HYDRUS code for simulating the movement of water, heat, and multiple

308   solutes in variably saturated porous media, 2005.

309   Steelman, C. M. and Endres, A. L.: An examination of direct ground wave soil moisture monitoring over an annual

310   cycle of soil conditions, Water Resour. Res., 46(11), n/a-n/a, doi:10.1029/2009WR008815, 2010.

311   Stork, C.: Reflection tomography in the postmigrated domain, Geophysics, 57(5), 680–692, doi:10.1190/1.1443282,

312   1992.

313   Topp, G. C., Davis, J. L. and Annan, A. P.: Electromagnetic Determination of Soil Water Content:, Water Resour.

314   Res., 16(3), 574–582, 1980.

315   Vellidis, G., Smith, M. C., Thomas, D. L. and Asmussen, L. E.: Detecting wetting front movement in a sandy soil

316   with ground-penetrating radar, Am. Soc. Agric. Eng., 33(6), 1867–1874, 1990.

317   Yilmaz, O. and Chambers, R.: Migration velocity analysis by wave-field extrapolation, Geophysics, 49(10), 1664–

318   1674, 1984.

319   Yilmaz, O. and Doherty, S.: Seismic Data Analysis: Processing, Inversion, and Interpretation of Seismic Data, 2nd

320   ed., Society of Exploration Geophysicists, Tulsa, OK., 2001.

321
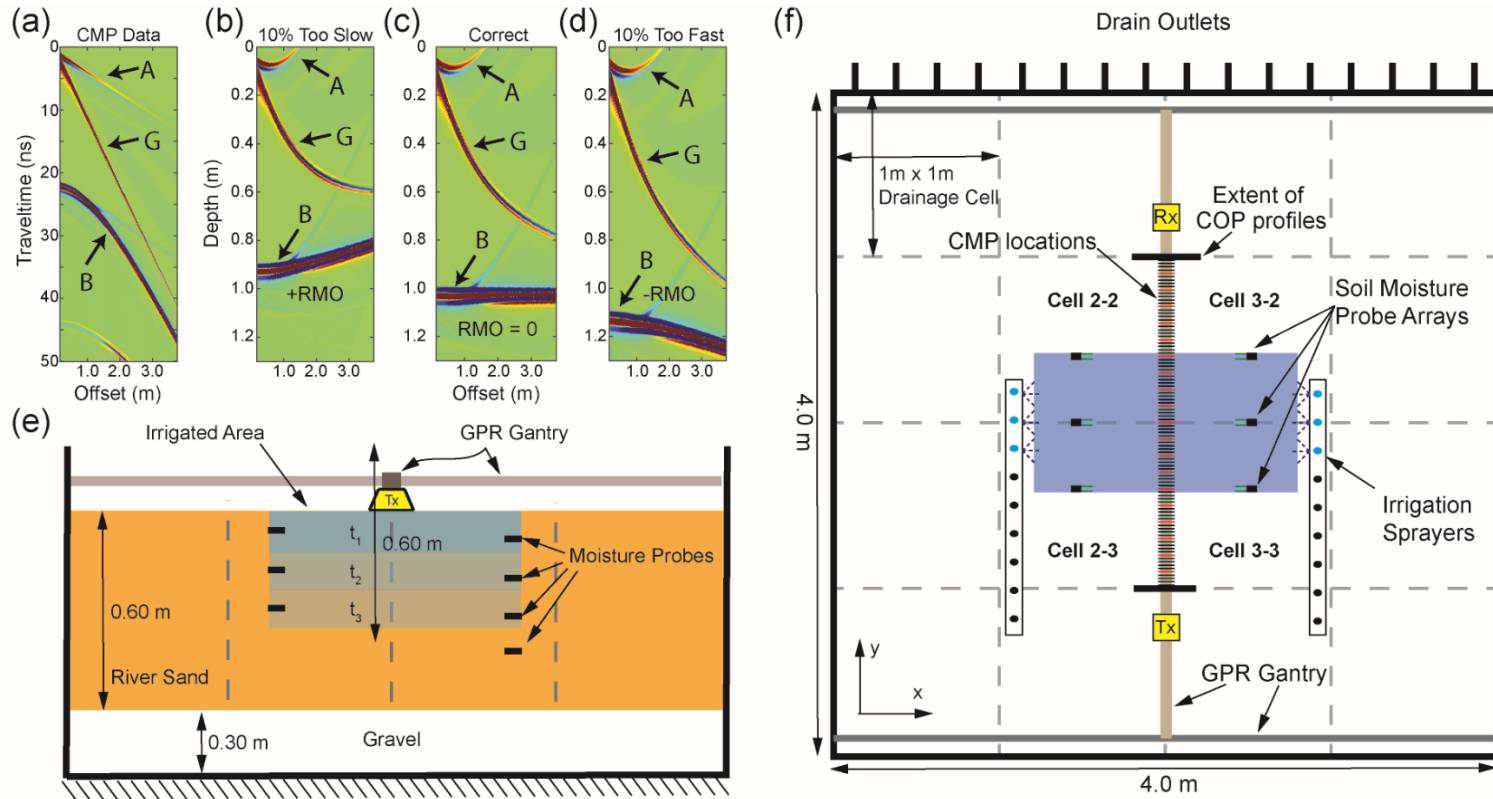
8. Figures

Figure 1

Figure 1: a) Example CMP data showing the airwave (A), groundwave (G) and reflection from a layer (B). Data in (a) is migrated to form (b) a migrated gather with velocity 10% too slow; c) a migrated gather with correct velocity; and d) a migrated gather with velocity 10% too fast. Panel (e) shows a cross-section of the experiment at y = 2.0 m where t_1, t_2, and t_3 are arbitrary times during the infiltration. Panel (f) shows the plan-view of the experiment. Note that the bottom of the sand layer is flat where GPR data collection occurs, i.e. on a boundary between drain cells, and pitched elsewhere toward cell drains.

329   **Figure 2**

330
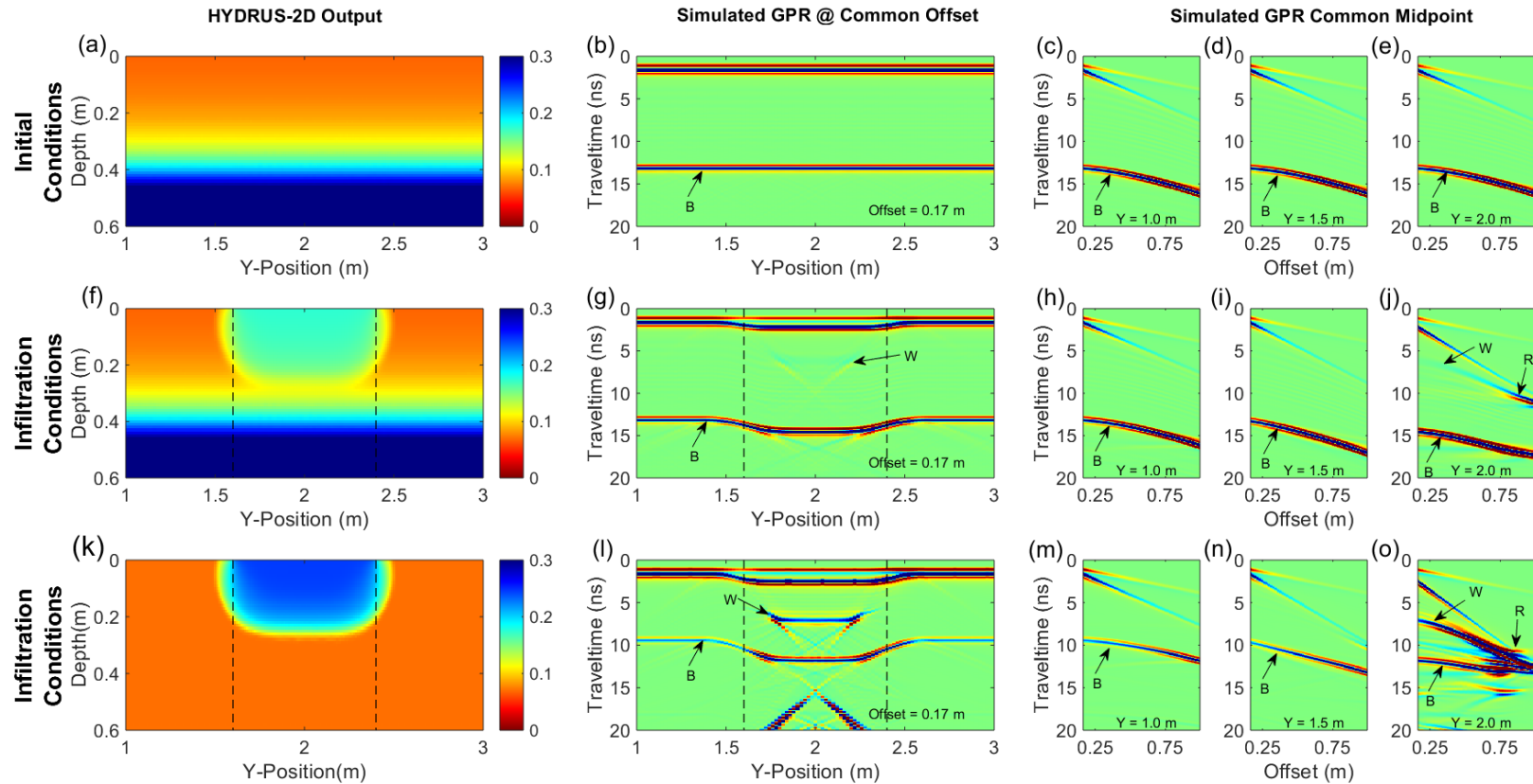
Figure 2: Panels (a), (f), and (k) show volumetric moisture distribution from HYDRUS-2D simulations used to generate simulated common-offset GPR data (b, g,
l) and multi-offset GPR data (c-e, h-j, and m-o). Vertical dashed lines indicate the extent of the wetted surface. Annotated arrivals are the bottom of sand layer
reflection (B), wetting front reflection (W), and refraction (R). Note that the base of sand reflection (B) is caused by the boundary at 0.60 m depth between the sand
and gravel, not the capillary rise shown in panels (a) and (f).

335   **Figure 3**
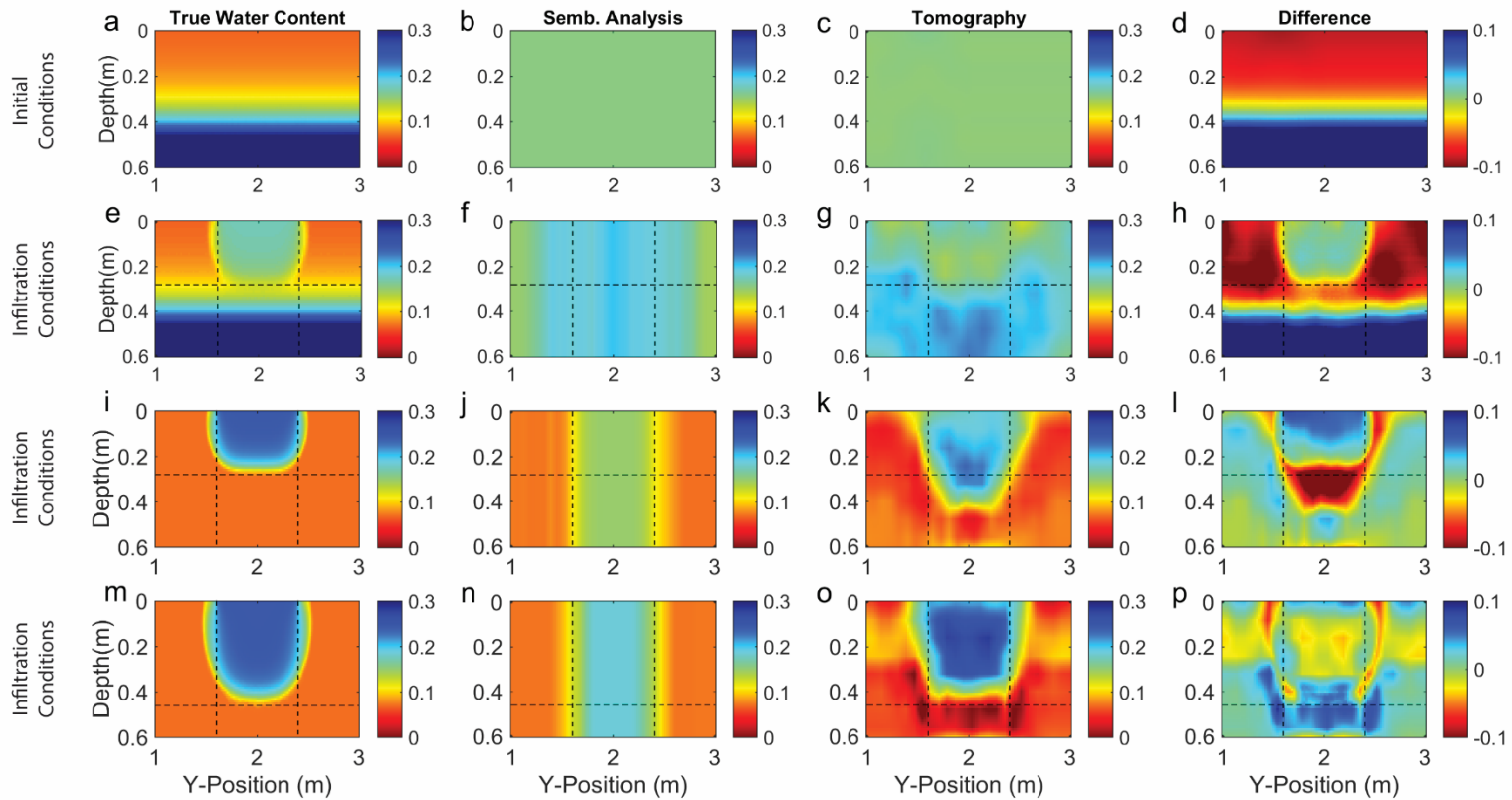
336

337   Figure 3: Panels (a), (e), ig), and (m) show true volumetric water content distributions from HYDRUS-2D. Panels (b), (f), (j), and (n) show starting models for the
338   tomography derived from semblance analysis. Panels (c), (g), (k), and (o) show results of tomography of the simulated GPR data as volumetric water content.
339   Difference plots (d), (h), (l), and (p) were calculated by subtracting the tomography results from the true water content distributions; red areas indicate volumetric
340   moisture overestimation while blue areas indicate volumetric moisture underestimation.

341

Figure 4

343
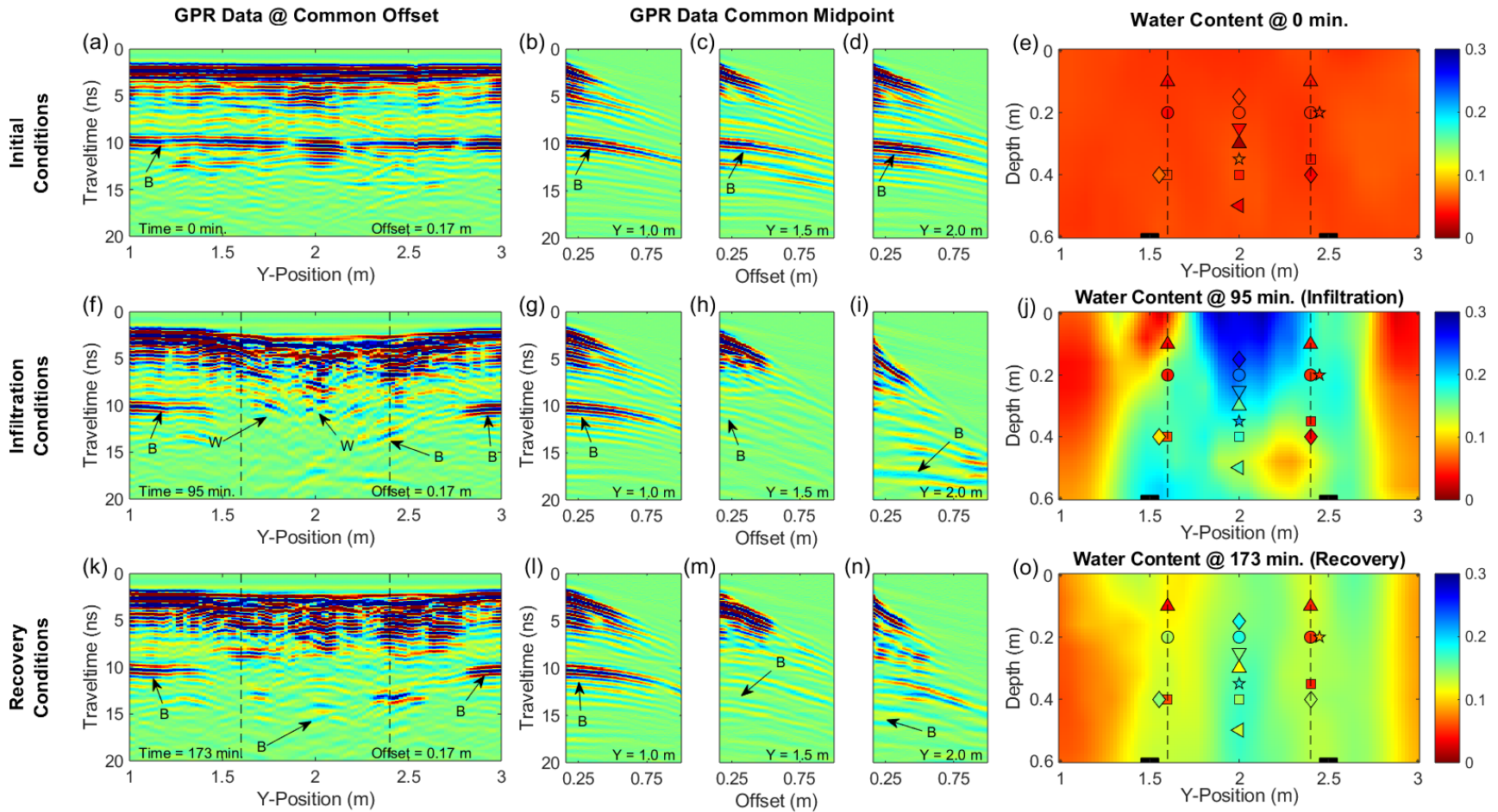
Figure 4: Panels (a, f, and k) are common-offset GPR data collected during the experiment. Panels (b-d, g-i, and l-n) are CMP data collected during the experiment.
Arrivals annotated are the sand layer reflection (B) and wetting front reflection (W). Panels (e, j, and o) show tomography results for the corresponding GPR data.
Vertical lines indicate the lateral extent of the wetted surface. Shapes correspond to the soil moisture data for the given y-location in Figure 5, colors correspond to
the measured soil moisture. Adjacent symbols are from probes that are located at different x-locations, but identical depths.

 Figure 5

349
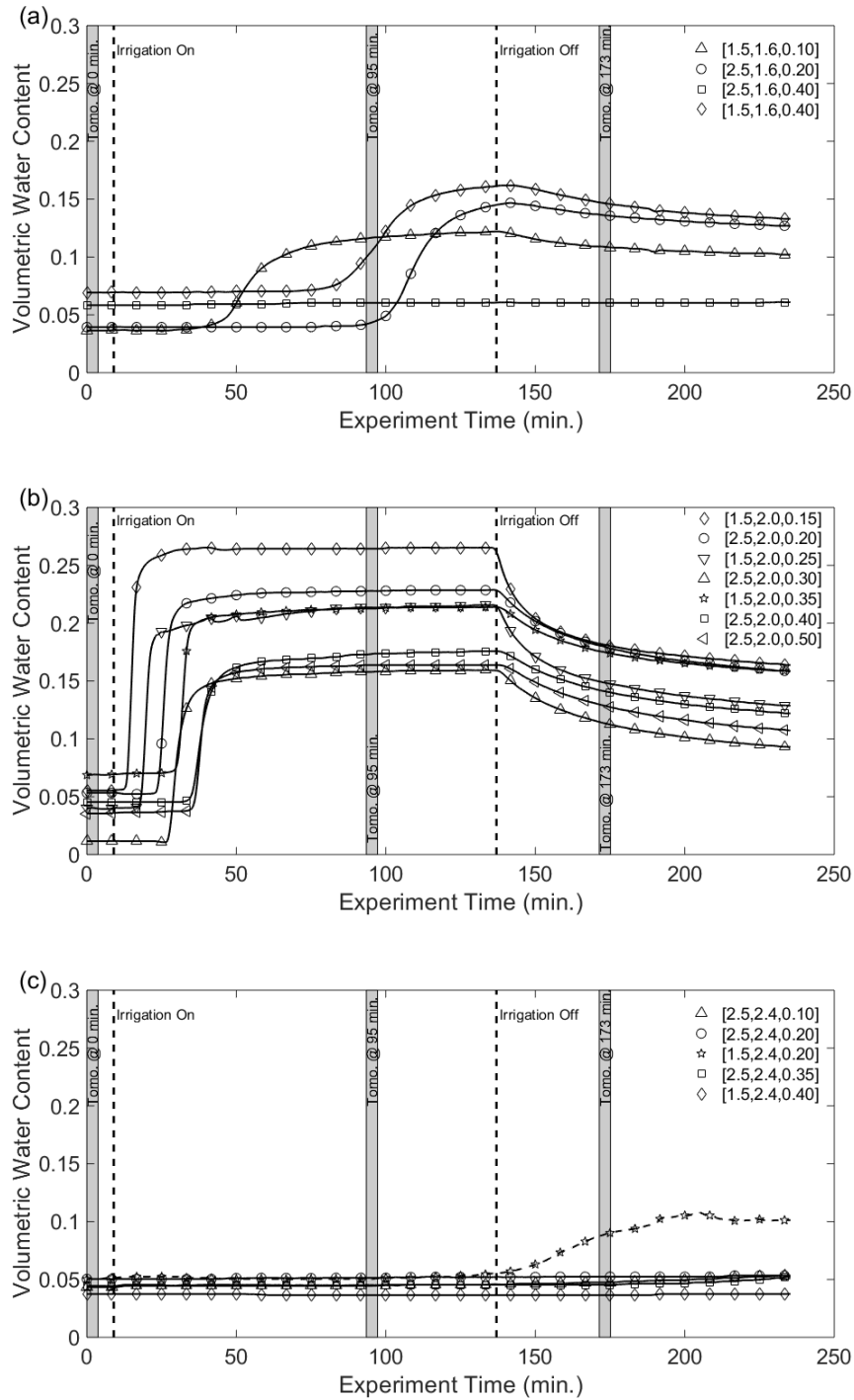
Figure 5: Soil moisture probe data from the in-situ moisture probes along the GPR line at a) y = 1.6 m; b) y = 2.0 m;
and c) y = 2.4 m. Vertical dashed lines indicate the start and stop of irrigation. Gray bars indicate the times when data
in Figure 4 were collected. Symbols for a given data set match those on Figures 4e, j, and o. Soil moisture data were
collected 60 minutes beyond the end of GPR data collection.